

**RIGOROUS ELECTROMAGNETIC MODELING OF RADIATIVE  
INTERACTION WITH MICROSTRUCTURES USING THE FINITE VOLUME  
TIME-DOMAIN METHOD<sup>1</sup>**

J. Liu<sup>2,3</sup>, S. J. Zhang<sup>4</sup>, and Y. S. Chen<sup>4</sup>

---

<sup>1</sup> Paper presented at the Fifteen Symposium on Thermophysical Properties, June 22-27, 2003, Boulder, Colorado, U. S. A.

<sup>2</sup> Taitech, Inc., WPAFB, OH 45433, U. S. A.

<sup>3</sup> To whom correspondence should be addressed. E-mail: [jiwenliu@msn.com](mailto:jiwenliu@msn.com)

<sup>4</sup> Engineering Sciences, Inc., Huntsville, AL 35802, U. S. A.

## **ABSTRACT**

A rigorous electromagnetic model is developed to predict the radiative properties of patterned silicon wafers. For nonplanar structures with characteristic length close to the wavelength of incident radiation, Maxwell's equations must be used to describe the associated radiative interaction and they are solved by the unstructured finite volume time-domain (FVTD) method. The basic idea of the FVTD method is to cast the two Maxwell curl equations in conservative form, and then treat the six scalar components of the electromagnetic fields as conserved quantities via a finite volume approach. In the die area, only one period of the structure is modeled due to its periodicity in geometry. To truncate a computational domain in an open space, the Mur boundary condition is applied to absorb outgoing waves. With the steady state time-harmonic electromagnetic fields known, the Poynting vector is used to calculate the radiative properties. To validate the present model, a wave scattering problem from a cylinder is considered at first and the predicted results are found to be essentially identical to the analytical solution. After that, radiative interactions with a nonplanar structure and a patterned wafer consisting of periphery and die area are investigated, and predicted reflectivities and absorptivities are found to match available other solutions very well, indicating that the present finite volume approach in the time domain is accurate to predict radiative interaction with microstructures.

**KEY WORDS:** finite volume time-domain method, Maxwell's equations, microstructures, radiative properties, silicon wafers.

## 1. INTRODUCTION

Rapid thermal processing (RTP) is a silicon wafer processing technology used to perform thermal operations in integrated circuit fabrication such as annealing, oxidation, or chemical vapor deposition (CVD) on a single wafer. Due to the continuous advances in microelectronics, RTP has been considered as a key manufacturing technology to replace batch furnace processing. The main advantage of RTP is that its lower thermal budget allows smaller devices to be made [1], which is difficult to achieve with batch heating. Despite this advantage, the wide acceptance of RTP in industry has been slowed due to the difficulty in achieving temperature uniformity across a wafer. Radiative heat transfer is the dominant mode of heat transfer in RTP systems and the wafer radiative properties have a first order effect on the wafer temperature uniformity. The reflectivity and absorptivity of the patterned silicon wafer are known to depend not only on the wavelength and temperature but also on the microstructures of dies which can include different materials, steps, trenches and bumps [2]. Because the characteristic length of these structures is close to wavelength of incident and emitted radiation, the interaction of radiation with the wafer must be described by the electromagnetic theory governed by Maxwell's equations while the traditional geometric optics (assuming that the characteristic length is much greater than the wavelength) and Rayleigh's method (assuming that the wavelength is much greater than the characteristic length) is no longer valid.

Maxwell's equations consist of up to six coupled partial differential equations and they are usually very difficult to be solved for realistic problems. Currently, most RTP system simulations employ simplified description of interaction of radiation from lamps with the wafer. Constant emissivity of the wafer is used in some models; in other a stack of

planar layers (thin films) on the wafer is taken into account. Actual microstructures of wafer surface, however are essentially nonplanar and nonuniform and include different materials with different optical properties as shown in Fig. 1. Therefore, rigorous 2D or 3D electromagnetic modeling is essential for an accurate prediction of radiative properties of the patterned silicon wafers. So far there have been very few studies available which solved the multi-dimensional Maxwell equations for prediction of radiative properties. Erofeev et. al. [2] were the first to model the radiative properties of 2D periodic surfaces with multilayers. They solved Maxwell's equations at the normal direction with frequency-domain finite element method. Wong et. al. [3-4] used the finite difference time-domain (FDTD) method to solve the multi-dimensional Maxwell equations for photolithographic applications. Their results of interest were the aerial images of the structure instead of the radiative properties of a wafer. Very recently, Liu et. al. [5] employed the FDTD method to model the interaction of radiation with the multilayered nonplanar microstructures from the patterned wafer. Their study showed that the rigorously electromagnetic model was essential to accurately predict the radiative properties in the die area. Compared to the frequency-domain methods, the time-domain approaches have an advantage that time step can be chosen sufficiently small so that electromagnetic wave scattering effects come only from neighboring nodes, the solution is thus found by time marching. This approach avoids the solving of a large matrix in most frequency-domain methods. In addition, the time-domain approaches can model either steady or unsteady time-harmonic electromagnetic fields while the frequency-domain methods are only limited to the steady case.

The objective of this study is to predict the radiative properties of patterned silicon wafer by solving the multi-dimensional Maxwell equations using the unstructured finite

volume time-domain (FVTD) algorithm. From our knowledge, this study represents the first to employ the FVTD method to rigorously model the interaction of radiation with the multilayered nonplanar microstructures from the patterned wafer. The most popular algorithm in solving Maxwell's equations in the time domain is undoubtedly the FDTD method developed by Yee [6]. This method applies the uncollocated electric and magnetic fields in both space and time. It was originally developed on uniform Cartesian grid, and later was extended to handle body-fitted grids [7, 8]. During the last three decades, the FDTD method has been successfully applied for a wide variety of science and engineering problems, including radar cross sections, antenna design, microwave circuits, bio-electromagnetic analysis, power generation and transmission, etc. In 1989, Shankar, et. al. [9] developed the FVTD method, which solved Maxwell's equations using a cell-centered finite volume scheme with a CFD-like Riemann solver approach. The FVTD method collocates the electric and magnetic fields in both space and time, rather than assigning them to two interleaved spatial grids and separating them one-half time step as used in the FDTD method. This has the advantage of reducing the complexity in gridding, in representing material regions, and in extracting near-field for transformation to the far field. Also, due to its control volume formulation, the FVTD method can easily handle body-fitted grids. More recently, this method was further refined and extended to unstructured grid [10-12]. With the unstructured grid technology, grid generation for complex geometries can be completely automated.

In this paper, the governing equations and discretization strategy will be presented at first, then the boundary conditions associated with the die area of a patterned wafer will be discussed. Followed will be the explanation of radiative properties calculation from the

electromagnetic fields. Finally, several benchmark problems involving nonplanar structures will be investigated to check the accuracy of the developed model. It should be stressed that even though the present study is focused on the RTP systems, it can be directly applied to many other problems such as spectroscopic instruments, optical property measurement, surface contamination, etc., where radiative reflection from rough and patterned thin film surfaces is a prominent phenomenon.

## 2. FINITE VOLUME FORMULATION OF MAXWELL'S EQUATIONS

The time-domain Maxwell equations in their vector form can be written as

$$\frac{\partial \mathbf{Q}}{\partial t} + \nabla \times \mathbf{L} = -\mathbf{M} \quad (1)$$

where

$$\mathbf{Q} = \begin{bmatrix} \mathbf{D} \\ \mathbf{B} \end{bmatrix} \quad (2)$$

contains the electric and magnetic flux density vectors, and

$$\mathbf{L} = \begin{bmatrix} -\mathbf{H} \\ \mathbf{E} \end{bmatrix} \quad (3)$$

contains the magnetic and electric intensity vectors, and

$$\mathbf{M} = \begin{bmatrix} \mathbf{J} \\ \mathbf{0} \end{bmatrix} \quad (4)$$

contains the electric current density vector. The vectors  $\mathbf{D}$  and  $\mathbf{H}$  are related to  $\mathbf{E}$  and  $\mathbf{B}$

by the constitutive relations

$$\begin{aligned} \mathbf{D} &= \varepsilon \mathbf{E} \\ \mathbf{B} &= \mu \mathbf{H} \end{aligned} \quad (5)$$

where  $\varepsilon$  is the permittivity and  $\mu$  is the permeability of the material. The electric current density  $\mathbf{J}$  is related to the electric intensity  $\mathbf{E}$  by

$$\mathbf{J} = \sigma \mathbf{E} \quad (6)$$

where  $\sigma$  is the electric conductivity of the material.

In solving Eq. (1) with a finite volume scheme, we first need to discretize the computational domain into small control volumes. For geometric flexibility, the control volume cells are arranged in an unstructured manner as seen in Fig. 2. The cell types vary from triangular or quadrilateral for 2D problems and tetrahedral, prism, pyramid, to hexahedral for 3D problems. The cell type in each problem can be single or mixed. With the domain discretization, we can obtain the following the discretized Maxwell equations by integrating Eq. (1) over an arbitrary control volume and also applying the divergence theorem,

$$\frac{\partial \mathbf{Q}}{\partial t} dV + \sum_{i=1}^N \mathbf{n}_i \times \mathbf{L}_i dS_i = \mathbf{M} dV \quad (7)$$

where  $dV$  is the volume of the control volume,  $N$  is the face number of the volume cell,  $\mathbf{n}_i$  is the unit normal of the face  $i$  of the control volume,  $dS_i$  is the area of the face  $i$ . Each control volume has a cell-averaged  $\mathbf{Q}$  vector, which is assumed to be the point  $\mathbf{Q}$  vector at the cell centroid. It is easy to see that the face tangential components of the electric and magnetic fields determine the time variation of the volume averaged electromagnetic fields. It is well known that a simple central difference-type method for Eq. (7) results in odd-even decoupling. Instead, CFD-type upwind schemes based on a Riemann solver or intensity-vector splitting [9, 13] are implemented for unstructured grids. This method can be divided

into three components: reconstruction, intensity-vector computation and time integration, which are presented in the following paragraphs.

### **Reconstruction**

In a cell centered finite volume procedure, the field variables are known in a cell-averaged sense. No indication is given as to the distribution of the solution over a control volume. In order to evaluate the intensity vector at a face, the field variables are required at both sides of the face. This task is fulfilled by reconstruction. A least squares reconstruction method is selected in this study. This reconstruction is capable of preserving a linear function on an arbitrary grid. Given an arbitrary field variable  $q$ , the gradients of  $q$  are constructed by the following least squares reconstruction

$$\begin{bmatrix} q_x \\ q_y \\ q_z \end{bmatrix} = \frac{1}{\Delta} L \begin{bmatrix} \sum (q_n - q_c)(x_n - x_c) \\ \sum (q_n - q_c)(y_n - y_c) \\ \sum (q_n - q_c)(z_n - z_c) \end{bmatrix} \quad (8)$$

where

$$\begin{aligned} \Delta &= I_{xx}(I_{yy}I_{zz} - I_{yz}^2) + I_{xy}(2I_{xz}I_{yz} - I_{xy}I_{zz}) - I_{xz}^2I_{yy} \\ I_{xx} &= \sum_n (x_n - x_c)^2; \quad I_{yy} = \sum_n (y_n - y_c)^2; \quad I_{zz} = \sum_n (z_n - z_c)^2 \\ I_{xy} &= \sum_n (x_n - x_c)(y_n - y_c); \quad I_{yz} = \sum_n (y_n - y_c)(z_n - z_c); \quad I_{xz} = \sum_n (x_n - x_c)(z_n - z_c) \end{aligned} \quad (9)$$

and

$$L = \begin{bmatrix} I_{yy}I_{zz} - I_{yz}^2 & I_{xz}I_{yz} - I_{xy}I_{zz} & I_{xy}I_{yz} - I_{xz}I_{yy} \\ I_{xz}I_{yz} - I_{xy}I_{zz} & I_{xx}I_{zz} - I_{xz}^2 & I_{xy}I_{xz} - I_{xx}I_{yz} \\ I_{xy}I_{yz} - I_{xz}I_{yy} & I_{xy}I_{xz} - I_{xz}I_{yz} & I_{xx}I_{yy} - I_{xy}^2 \end{bmatrix} \quad (10)$$

where  $n$  indicates the supporting neighbor cell,  $c$  denotes the current cell, and  $x, y, z$  are the cell centroid coordinates. It can be observed that the matrixes  $L$  and  $\Delta$  are dependent on the

geometry only. If we store  $I_{xx}$ ,  $I_{yy}$ , etc., the reconstruction can be performed efficiently with one loop over the neighboring cells.

### **Intensity-vector Computation**

After the cell-wise reconstruction, the field variables at the left and right side of any face can be determined based on a simple Taylor expansion, i. e.,

$$\mathbf{Q}_{fL} = \mathbf{Q}_L + \nabla \mathbf{Q}_L \cdot (\mathbf{r}_f - \mathbf{r}_L) \quad (11)$$

$$\mathbf{Q}_{fR} = \mathbf{Q}_R + \nabla \mathbf{Q}_R \cdot (\mathbf{r}_f - \mathbf{r}_R) \quad (12)$$

where  $\mathbf{r}_f$  is the position vector of the face center,  $\mathbf{r}_L$  and  $\mathbf{r}_R$  are the position vectors of the left and right cell centroids. Then the intensity vector at the face is computed based on a Riemann solver [9]. Given the left and right field variables, the intensity vector at the face can be expressed as

$$\mathbf{L}_f = \left[ \begin{array}{c} \frac{(\mu c)_R \mathbf{H}_R + (\mu c)_L \mathbf{H}_L - \mathbf{n} \times (\mathbf{E}_R - \mathbf{E}_L)}{(\mu c)_R + (\mu c)_L} \\ \frac{(\mu c)_R \mathbf{E}_R + (\mu c)_L \mathbf{E}_L + \mathbf{n} \times (\mathbf{H}_R - \mathbf{H}_L)}{(\mu c)_R + (\mu c)_L} \end{array} \right] \quad (13)$$

where  $c$  is the wave speed and equal to  $1/\sqrt{\epsilon\mu}$ .

### **Time Integration**

Once the intensity vector is determined at each face of a control volume, a time integration scheme is then needed for Eq. (7) to advance the unknowns in time. In this study, the following fourth-order, four-stage explicit Runge-Kutta scheme is used to integrate Eq. (7) in the  $(n+1)$ -th time step with a time step  $\Delta t$

$$\mathbf{Q}^{n+1} = \mathbf{Q}^n + \frac{\Delta t}{6} (\mathbf{f}^n + 2\mathbf{f}^* + 2\mathbf{f}^{**} + \mathbf{f}^{***}) \quad (14)$$

where

$$\mathbf{f} = \mathbf{M} - \frac{1}{dV} \sum_{i=1}^N \mathbf{n}_i \times \mathbf{L}_i dS_i \quad (15)$$

and

$$\begin{aligned} \mathbf{Q}^* &= \mathbf{Q}^n + \frac{\Delta t}{2} \mathbf{f}^n; & \mathbf{f}^* &= \mathbf{f}(t^{n+1/2}, \mathbf{Q}^*) \\ \mathbf{Q}^{**} &= \mathbf{Q}^n + \frac{\Delta t}{2} \mathbf{f}^*; & \mathbf{f}^{**} &= \mathbf{f}(t^{n+1/2}, \mathbf{Q}^{**}) \\ \mathbf{Q}^{***} &= \mathbf{Q}^n + \Delta t \mathbf{f}^{**}; & \mathbf{f}^{***} &= \mathbf{f}(t^{n+1}, \mathbf{Q}^{***}) \end{aligned} \quad (16)$$

### 3. NUMERICAL TREATMENT OF BOUNDARY CONDITIONS

For the application of FVTD method, the computational domain must be confined by some means due to computer memory and CPU limitations. It is known the die area of a patterned wafer usually shows a periodic geometric profile. So only a single period of the structure in the x-direction needs to be modeled in the die area as shown in Fig. 3. In the y direction, the die area is exposed to free space and a considerably thick substrate (compared to the structure), two artificial boundaries must be introduced to truncate the free space and substrate, and they are usually called the absorbing boundary conditions. Ideally, the absorbing boundaries should not affect the propagation of electromagnetic waves, i. e., they should annihilate the outward-going waves without any reflection. A typical computational domain containing periodic and absorbing boundary conditions is shown in Fig. 4 and it is excited at the top by a monochromatic plane wave.

For a periodic structure, the amplitudes of the field components are equal at the left and right boundaries (Fig. 4). If the phase differences of the field components between the two sides are also equal to  $2\pi m$  (where  $m$  is any integer), the field components are periodic function along the x-direction and the boundary conditions can be easily implemented at the

left and right sides. It is noted that the periodic boundary condition is not automatically satisfied in a periodic structure. In some RTP systems, the incident radiation mainly comes from the normal direction. At this condition, the phases of the field components between the two sides are equal, the periodic condition is applied to each field component. For some RTP systems, the effect of oblique incidence may have to be taken into account. At such a situation, the periodic condition is applied only if the incident angle  $\theta$  is

$$\theta = \sin^{-1}\left(\frac{m\lambda}{d}\right) \quad (17)$$

where  $d$  is the horizontal period of a periodic structure and  $\lambda$  is the incident wavelength. The numerical treatment of general oblique incidence is possible for a periodic structure, however it is very tedious. Implementation of general oblique incidence will be one of our studies in the future.

For an open radiation problem, one of the most commonly used absorbing boundary condition is the Mur boundary condition [14] and it is applied in this study. The Mur boundary condition is based on the one-way approximation of the wave equation initially exhibited for acoustic wave by Engquist and Majda [15]. This condition is very easy to implement and it absorbs a wave without reflection if the wave is plane and propagates perpendicularly to the boundary. More accurate absorbing boundary conditions such as the perfectly matched layer (PML) [16-18] technique are available and their implementation in the FVTD method will be also one of the future studies.

#### **4. PREDICTION OF RADIATIVE PROPERTIES**

The FVTD method calculates the transient electromagnetic fields throughout the computational domain under the excitation of a monochromatic harmonic field. However,

the real results of interest in this study are the radiative properties and they are associated with the electromagnetic fields through the wave intensity. The intensity of the harmonic wave is defined as a mean value of the Poynting vector and expressed as

$$\mathbf{I}(x, y) = \frac{1}{T^*} \int_0^{T^*} \mathbf{E} \times \mathbf{H} | dt \quad (18)$$

where  $T^* = 2\pi/\omega$  is the time period of the wave. Then the reflectivity is defined as a ratio of the reflected and incident intensities and the transmissivity is defined as a ratio of the transmitted and incident intensities. For the transverse electric (TE) polarization, the reflectivity  $R_e$  is calculated at an arbitrary constant  $y$  plane above the die structure and has the following form:

$$R_e = \frac{\int_a^d \int_b^{T^*} |\mathbf{E} \times \mathbf{H}| dt dx}{\int_a^d \int_b^{T^*} |\mathbf{E}_{in} \times \mathbf{H}_{in}| dt dx} \quad (19)$$

where the incident electric and magnetic fields  $\mathbf{E}_{in}$  and  $\mathbf{H}_{in}$  are provided by a user and  $\mathbf{E}$  and  $\mathbf{H}$  are calculated by the FVTD method discussed previously. For unpolarized wave, its reflectivity is taken to be an arithmetic average of the reflectivities from TE and transverse magnetic (TM) polarizations, that is,

$$R = 0.5(R_e + R_m) \quad (20)$$

With  $R$  given, the corresponding transmissivity  $T$  becomes

$$T = 1 - R \quad (21)$$

In some RTP simulations, the apparent radiative properties are the quantities of interest and they take into account reflection from the wafer backside. To predict these properties, we calculate firstly reflectivity  $R_b$  of the wafer backside using the thin film

theory [19] since we assume backside film structure to be planar. If the absorption coefficient of the substrate is  $\alpha$  and the wafer thickness is  $H_w$ , then the apparent absorptivity of the wafer (or its emissivity as it follows from the equilibrium condition) is

$$A_0 = (1 - R)[1 - \exp(-\alpha H_w)][1 + R_b \exp(-\alpha H_w)] \quad (22)$$

This expression is often used to calculate the heat absorbed by the wafer.

## 5. RESULTS AND DISCUSSION

Based on the above numerical approach, a computer code has been developed which is capable of simulating propagation of 2D and 3D electromagnetic wave in lossy, anisotropic, and inhomogeneous mediums with irregular geometries by using an unstructured FDTD method. To examine the performance of the present code, several problems containing different geometries are investigated and they are all assumed to be excited by a sinusoidal plane wave. So far, the FDTD method has been mainly applied for electromagnetic scattering problems. So we first consider a wave scattering by a conducting cylinder. After that, we investigate electromagnetic wave interaction with several non-planar structures with characteristic sizes close to the wavelength of radiation. For each problem, the grid resolution is usually more than 20 points per wavelength in order to obtain grid independent results. In this study, all computations were conducted on the 800 MHz Linux PC machine. For a typical simulation, the steady-state harmonic solution is reached after 10 wave cycles. The corresponding CPU time is dependent on the problem size and it is usually not more than an hour.

## 5.1 Wave scattering by a conducting cylinder

Consider a TE plane wave incident on a perfect conducting cylinder. This problem is selected because its analytical solution exists. For a perfect electrical conductor, the tangential components of the electric field must be zero on the conductor surface. Figure 5(a) shows the unstructured grid used in the calculation. The incident TE plane wave has a wave number of  $1 \text{ m}^{-1}$  with the magnetic field intensity amplitude of  $3.0 \times 10^8 \text{ A/m}$ . The radius of the cylinder is 1.0 m. The open boundary is located about two wave lengths away from the cylinder. In the computation, a scattered wave formulation was employed instead of the total wave formulation. The time step was chosen to be  $1.0 \times 10^{-10}$  second. Figure 5(b) demonstrates the nondimensional electric current profile along the cylinder surface. The present results are found to be essentially identical to the exact solution [20], indicating that our developed Maxwell's equation solver is very accurate.

## 5.2 Radiative interaction with a non-planar structure

With the validation of the present code in electromagnetic wave scattering problems, we shift our attention on radiative interaction with microstructures. The interaction of radiation wave with planar structures is well-known and the corresponding reflectivity and transmissivity can be easily calculated from the thin film theory [19]. Electromagnetic wave interaction with a non-planar structure with characteristic length close to the wavelength of radiation is much more complicated than that with a planar structure. As a result, it is impossible to use the exact method to predict the associated radiative properties. So far there have been very few studies available which involved solving Maxwell's equations to calculate the reflection, transmission, and absorption coefficients. Erofeev et. al. [2] were

the first to rigorously model radiative properties of non-planar structures for comprehensive RTP simulation by solving Maxwell's equation using the frequency-domain finite element method. One of their considered problems is a periodic structure consisting of trenches and juts shown in Fig. 6 and it will be investigated by the present code for the validation study. The structure is assumed to be illuminated at normal direction with wavelength at  $1.0 \mu\text{m}$  (maximum of radiation spectrum at the filament temperature  $3000 \text{ K}$  in a RTP system) and it is maintained at a temperature of  $600 \text{ C}$ . The period of the structure is  $2.0 \mu\text{m}$  and the trench depth can be changed from  $0$  to  $1.0 \mu\text{m}$ . Before Maxwell's equations are solved, the material parameters  $\varepsilon$  and  $\sigma$  are calculated from the complex refractive index. The complex refractive index of silicon depends on wavelength, temperature and impurity concentration and it is taken from Refs. [21, 22].

Table 1 shows the calculated reflectivities at different trench depths based on a domain  $2.0 \mu\text{m} \times 4.0 \mu\text{m}$  which is discretized into  $80,000$  quadrilateral volume cells. The result of interest is the relectivity of nonpolarized wave rather than that for specific polarization. The reflectivities from Erofeev et. al. [2] in the table are directly hand picked from the paper and they may be subjected to small errors. So, the results are considered to be meaningful only to the third decimal place. Previously, the present authors applied the FDTD method [5] to investigate the same problem and their results are also listed in the Table 1 for comparison. As the trench depth is increased from  $0$  to  $1.0 \mu\text{m}$ , the calculated reflectivity is seen to keep changing. At  $h=0.75 \mu\text{m}$ , the reflectivity drops over  $15\%$  in comparison with that at  $h=0 \mu\text{m}$ . Compared to the studies from Erofeev et. al. and FDTD method, the present prediction basically shows a good agreement for each case. The maximum relectivity difference among three different studies is around  $5\%$ .

### 5.3 Radiative interaction with a patterned wafer

With the validation of the present code in a nonplanar structure, a complete patterned wafer shown in Fig. 7 will be investigated to demonstrate how the radiative properties change across the wafer. The front side of the wafer consists of the wafer periphery and die area. The periphery area can be considered as a planar structure and it is 50 nm layer of  $\text{Si}_3\text{N}_4$  deposited on the silicon substrate. The die area has a periodic structure similar to those in Fig. 6 but silicon surface is covered with 50 nm  $\text{Si}_3\text{N}_4$  layer. The trench depth can be changed from 0 to 1.0  $\mu\text{m}$ . The substrate thickness equals 0.7 mm, and wafer temperature equals 600 C. The wavelength of incident radiation is set to be 1.0  $\mu\text{m}$ . In the present computation, the complex reflective index of  $\text{Si}_3\text{N}_4$  is taken from Ref. [21]. The sizes of the computational domain for the periphery and die areas are chosen to the same and they are 2.0  $\mu\text{m} \times 4.0 \mu\text{m}$ . The total numbers of quadrilateral cells used for two domains are also the same and they are equal to 800,000. Like the previous problem, this problem was also considered previously by the present author with the FDTD method [5] and the corresponding solution will be used to examine the accuracy of the present results from the FVTD method.

Table 2 shows the apparent absorptivities from the periphery and die region with varying trench depth at normal incidence. For comparison, the apparent absorptivities from the bare silicon are also provided. In the last two decades, prediction of wafer radiative properties has experienced three developmental stages. In the first stage, an entire wafer is treated simply as bare silicon. In the second stage, both the periphery and die region are treated as thin film structures. The third stage involves rigorously electromagnetic modeling as described in this study. As the stage number changes from one to three, the accuracy of

predicted radiative properties across a wafer should be increased because the physical model becomes more realistic. In the wafer periphery, the present results (third column) are almost identical to the results from the thin film theory (not listed) because the considered structure is of planar geometry. However, the bare silicon approach (second column) underestimates the absorptivities by about 11% in the wafer periphery. In the die area, the thin film approach calculates the radiative properties of each component at first, these properties are then averaged using the fractional area of the components as weighting factors. The die area shown in Fig.7 consists of two components, silicon substrate and substrate coated with  $\text{Si}_3\text{N}_4$ , and the corresponding thin film results are listed in the fourth column of the table. Obviously, the thin film approach cannot consider the effect of varying trench depth. Compared to the results by directly solving Maxwell's equations, the thin film approach underestimates the absorptivities by up to 6% with  $h=0.5 \mu\text{m}$  in the die area. This level of difference in radiative properties will have a great implication on the wafer temperature distribution. Compared to the results from the FDTD method, the present prediction shows a very good agreement for each case. The maximum absorptivity difference between two different methods is within 2%.

## **6. CONCLUSIONS**

Since real microstructures of dies are nonplanar and have characteristic length close to the wavelength of incident radiation, a rigorous electromagnetic model has been developed to solve Maxwell's equations using the FVTD method and predict the radiative properties of patterned silicon wafers. To validate the present model, a wave scattering problem is considered at first and the predicted results are found to be essentially identical to the

analytical solution. After that, radiative interactions with a nonplanar structure and a patterned wafer consisting of periphery and die area are investigated, and predicted reflectivities and absorptivities are found to match available other solutions very well, indicating that the present finite volume approach in the time domain is accurate to predict radiative interaction with microstructures.

## ACKNOWLEDGMENT

This project was partially supported by the National Sciences Foundation under contract DMI-0078608.

## REFERENCES

1. Hebb, P. J., Ph.D. Dissertation, Department of Mechanical Engineering, MIT, 1997.
2. Erofeev, A. F., Kolpakov, A. V., Makhviladze, T. M., Martjushenko, A. V., Panjukhin, A. V., Volchek, O. S., *Proceedings of 3<sup>rd</sup> International Rapid Thermal Processing Conference*, pp. 181-197, 1995.
3. Wong, A. K., Guerrieri, R., and Neureuther, A. R., *IEEE Trans. Computer-Aided Design*, Vol. 14, No. 10, pp. 1231-1240, 1995.
4. Wong, A. K. and Neureuther, R., *IEEE Trans. Semiconductor Manufacturing*, Vol. 8, No. 4, pp. 419-431, 1995.
5. Liu, J., Zhang, S. J. and Chen, Y. S., Accepted for publication in *Numerical Heat Transfer, Part B*.
6. Yee, K., S., *IEEE Trans. Antenn. Propagat.*, Vol. 14, No. 3, pp. 302-307, 1966.
7. Holland, R., *IEEE Trans. Nuc. Sci.*, Vol. NS-30, No. 6, pp. 4589-4591, 1983.
8. Fusco, M., *IEEE Trans. Antenn. Propagat.*, Vol. 38, No. 1, pp. 76-89, 1990.

9. Shankar, V., Hall, W., and Mohammadian, A. H., AIAA-89-1987-CP, 1989.
10. Liu, Y., Proceedings of 10<sup>th</sup> Annual Review of Progress in Applied Computational Electromagnetics, 1994.
11. Liu, Y., 1995 Digest, USNC/URSI Radio Science Meeting, 1995.
12. Hall, W. F., Shankar, V., and Palaniswamy, S., AIAA-97-2089, 1997.
13. Shang, J. S., *IEEE Trans. Antenn. Propagat.*, Vol. 43, No. 3, pp. 15-25, 1995.
14. Mur, G., *IEEE Trans. Electromagnetic Comp.*, Vol EMC-23, No. 4, pp. 377-382, 1981.
15. Engquist, B. and Majda, A., *Comm. On Pure and Applied Math.*, Vol. 32, pp. 313-357, 1979.
16. Berenger, J. P., *J. Computat. Phys.*, Vol. 114, pp. 185-200, 1994.
17. Sack, Z. S., Kingsland, D. M., Lee, R., and Lee, J. F., *IEEE Trans. Antennas Propagat.*, Vol. 43, pp. 1460-1463, 1995.
18. Gedney, S. D., *IEEE Trans. Antennas Propagat.*, Vol. 44, pp. 1630-1639, 1996.
19. Yeh, P., *Optical Waves in Layered Media*, Wiley, New York, 1988.
20. Harrington, R. F., *Time-Harmonic Electromagnetic Fields*, McGraw-Hill, New York, 1961.
21. Palik, E. D., *Handbook of Optical Constants of Solids*, Academic Press, New York, 1995.
22. Jellison, G. E. and Modine, F. A., *J. Appl. Phys.* Vol. 76, No. 6, pp. 3758-3761, 1994.

## LIST OF TABLES AND FIGURES

Table 1	Reflectivities of a nonplanar structure with varying trench depth
Table 2	Apparent absorptivities of a patterned wafer containing the periphery and die region with varying trench depth
Fig. 1	Schematic of a patterned wafer: (a) front side, which has the die area and wafer periphery, and (b) cutaway showing the profile of different areas.
Fig. 2	Cell centered control volume for 2D unstructured grids
Fig. 3	An example of nonplanar multilayered die structure
Fig. 4	Computational domain and boundary conditions
Fig. 5	Wave scattering by a conducting cylinder; (a) unstructured computational grid and (b) electric current distribution along the cylinder surface.
Fig. 6	A non-planar periodic structure with varying trench depth
Fig. 7	A patterned wafer containing the periphery and die region

Table 1 Reflectivities of a nonplanar structure with varying trench depth

h, $\mu\text{m}$ Solution	0.0	0.25	0.5	0.75	1.0
Present	0.337	0.289	0.297	0.282	0.301
Erofeev et. al	0.337	0.290	0.286	0.270	0.298
FDTD	0.335	0.297	0.280	0.277	0.301

Table 2 Apparent absorptivities of a patterned wafer containing the periphery and die region with varying trench depth

Structure Solution	Bare silicon	Wafer periphery	Die region (thin film)	Die region with varying trench depth h, $\mu\text{m}$				
				0.0	0.25	0.50	0.75	1.0
Present	0.6653	0.7517	0.7085	0.7079	0.7316	0.7558	0.7480	0.7448
FDTD	0.6653	0.7517	0.7085	0.7071	0.7233	0.7686	0.7379	0.7394

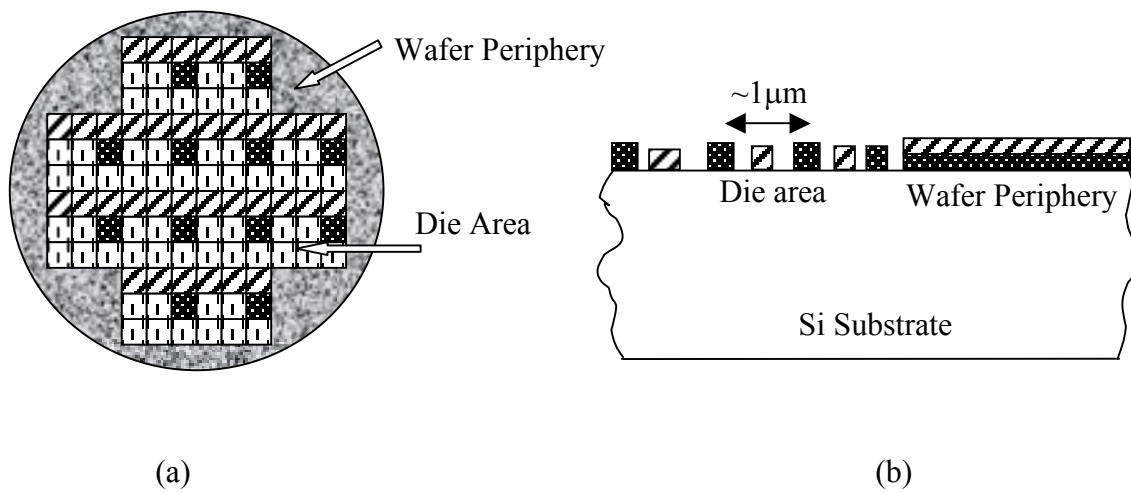


Fig. 1 Schematic of a patterned wafer: (a) front side, which has the die area and wafer periphery, and (b) cutaway showing the profile of different areas.

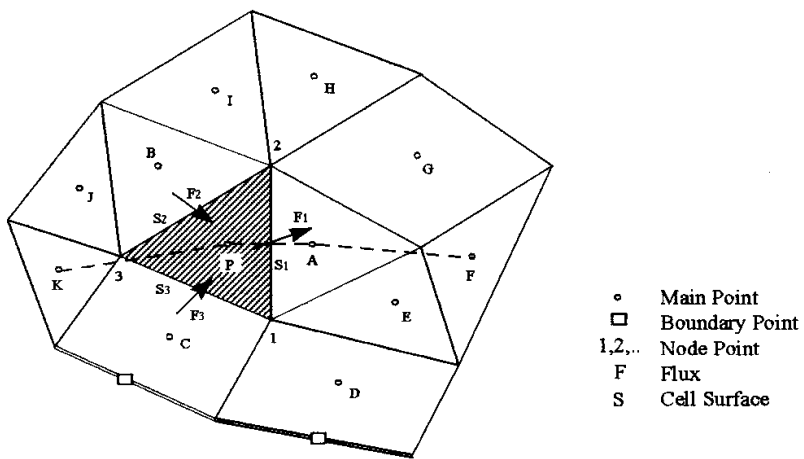


Fig. 2 Cell centered control volume for 2D unstructured grids

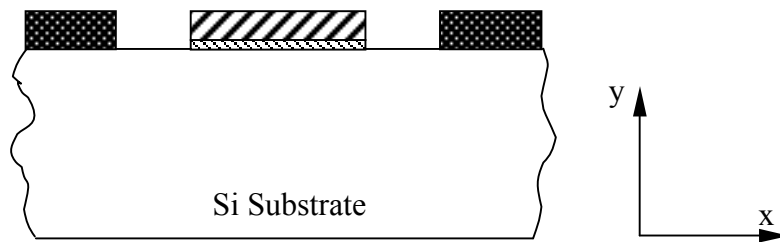


Fig. 3 An example of nonplanar multilayered die structure.

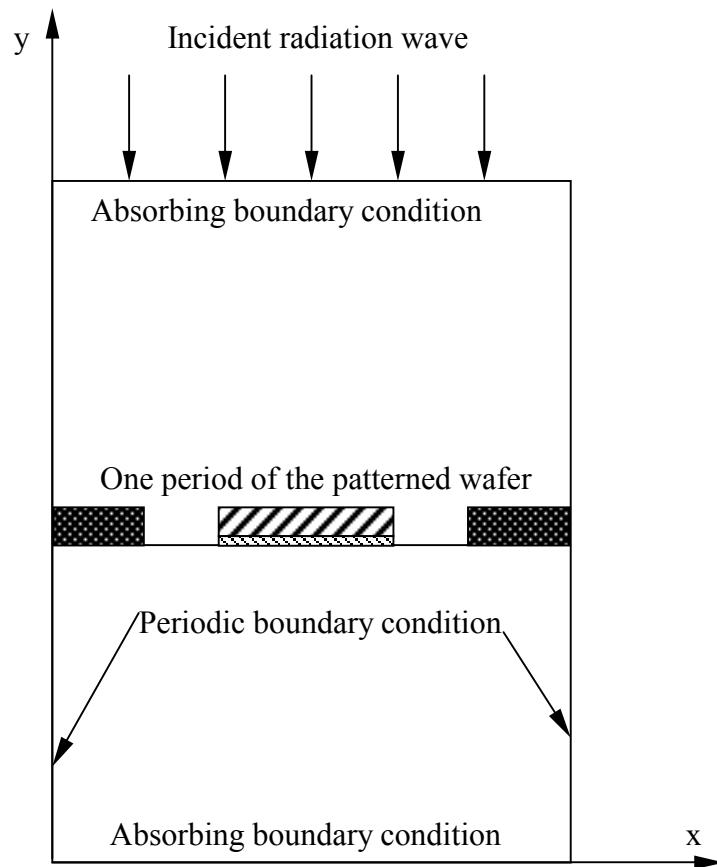
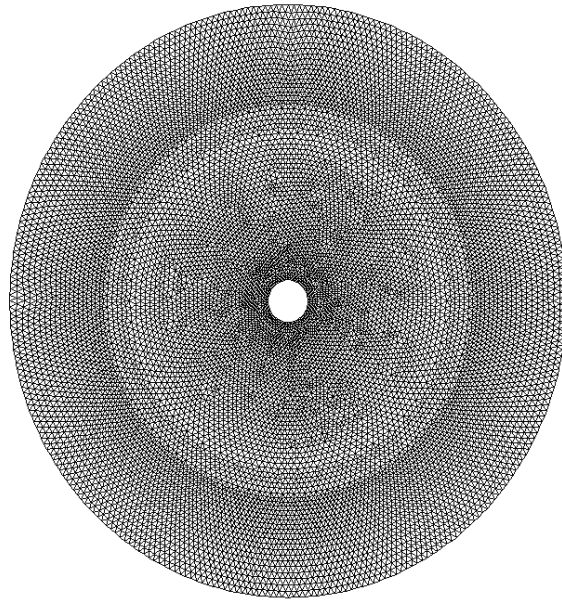
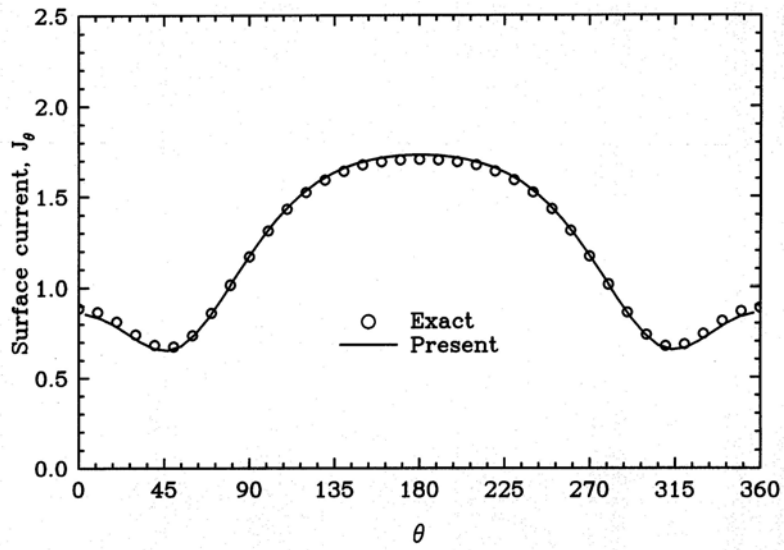


Fig. 4 Computational domain and boundary conditions.



(a)



(b)

Fig. 5 Wave scattering by a conducting cylinder; (a) unstructured computational grid and (b) electric current distribution along the cylinder surface.

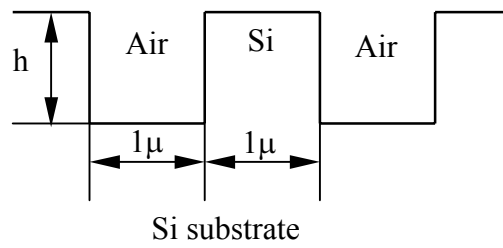


Fig. 6 A non-planar periodic structure with varying trench depth.

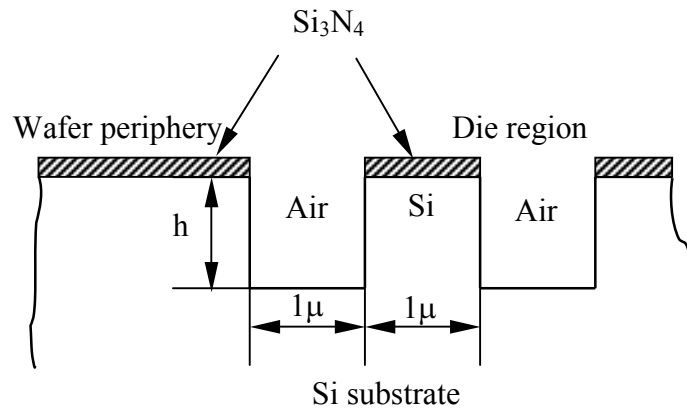


Fig. 7 A patterned wafer containing the periphery and die region.